Urban Climate 31 (2020) 100576

Contents lists available at ScienceDirect

Urban Climate

journal homepage: www.elsevier.com/locate/uclim

Heat risk mapping through spatial analysis of remotely-sensed data and socioeconomic vulnerability in Hermosillo, México

Javier Navarro-Estupiñan[a], Agustín Robles-Morua[a,*], Rolando Díaz-Caravantes[b], Enrique R. Vivoni[c,d]

[a] Departamento de Ciencias del Agua y Medio Ambiente, Instituto Tecnológico de Sonora, México
[b] Centro de Estudios en Salud y Sociedad, El Colegio de Sonora, Mexico
[c] School of Earth and Space Exploration, Arizona State University, United States of America
[d] School of Sustainable Engineering and the Built Environment, Arizona State University, United States of America

1. Introduction

Globally, urbanization has led to the expansion of impervious surfaces, which typically increases the magnitude and spatio-temporal variability of land surface temperature (LST). A range of factors contributes to the spatial heterogeneity of LST in cities (Lazzarini et al., 2015; Li et al., 2017; Peng et al., 2018). For example, the heterogeneous replacement of natural land covers with buildings, road pavements and other materials significantly alters the surface energy balance (Arnfield, 2003; Chow et al., 2014; Myint et al., 2015; Yang et al., 2017; Templeton et al., 2018). Unfortunately, the traditional means to characterize the urban heat island effect and its associated hazards through ground-based air temperature data is dependent on having a large number of climatic stations (Aina et al., 2017), which are lacking in many cities, in particular for developing countries such as México. Thus, urban heat hazards need to be identified through other mapping platforms.

Thermal remote sensing products present new opportunities to monitor LST in a spatially-distributed manner (Lo et al., 1997; Chen et al., 2006; Xiang et al., 2017; De Faria Peres et al., 2018). For instance, satellite-based LST measurements have been used to quantify the effect of land cover variations on thermal conditions (Jenerette et al., 2016; Wang et al., 2016; Azevedo et al., 2016; Ranagalage et al., 2017; Li et al., 2018), including studies conducted in México (García-Cueto et al., 2007; Cui and De Foy, 2012). As a result, it is now possible to relate LST to the properties of the built environment and the socioeconomic characteristics that vary spatially in a city. For instance, prior work in Phoenix, Arizona (Chow et al., 2012), has revealed strong linkages between LST, vegetation cover and income that can inform heat mitigation strategies.

In this study, satellite-based LST imagery from LandSat 8 is used to quantify urban temperatures in Hermosillo, México. Despite having a high incidence of heat-related mortalities (Díaz-Caravantes et al., 2014; Martínez-Austria and Bandala, 2017), there have been no prior efforts to quantify urban temperatures through satellite data and link these to socioeconomic indicators of heat vulnerability. To do this, we introduce the use of time stability (or persistence) analysis for LST, a technique shown to be effective in identifying above- and below-average regions in a map (Vachaud et al., 1985). Outcomes of the time stability analysis are used to indicate heat exposure, while a series of socioeconomic factors are used to identify the vulnerability of different social sectors to urban heat through a spatial clustering technique. The resulting heat risk map for Hermosillo is an effective planning tool for developing heat mitigation strategies, including the placement of green infrastructure, as well as an aid to communication campaigns during summer heat waves.

* Corresponding author at: Departamento de Ciencias del Agua y Medio Ambiente, Instituto Tecnológico de Sonora, 5 de Febrero 818 Sur Colonia Centro, Ciudad Obregón, Sonora 85000, México.
E-mail address: agustin.robles@itson.edu.mx (A. Robles-Morua).

https://doi.org/10.1016/j.uclim.2019.100576
Received 17 July 2019; Received in revised form 18 December 2019; Accepted 19 December 2019

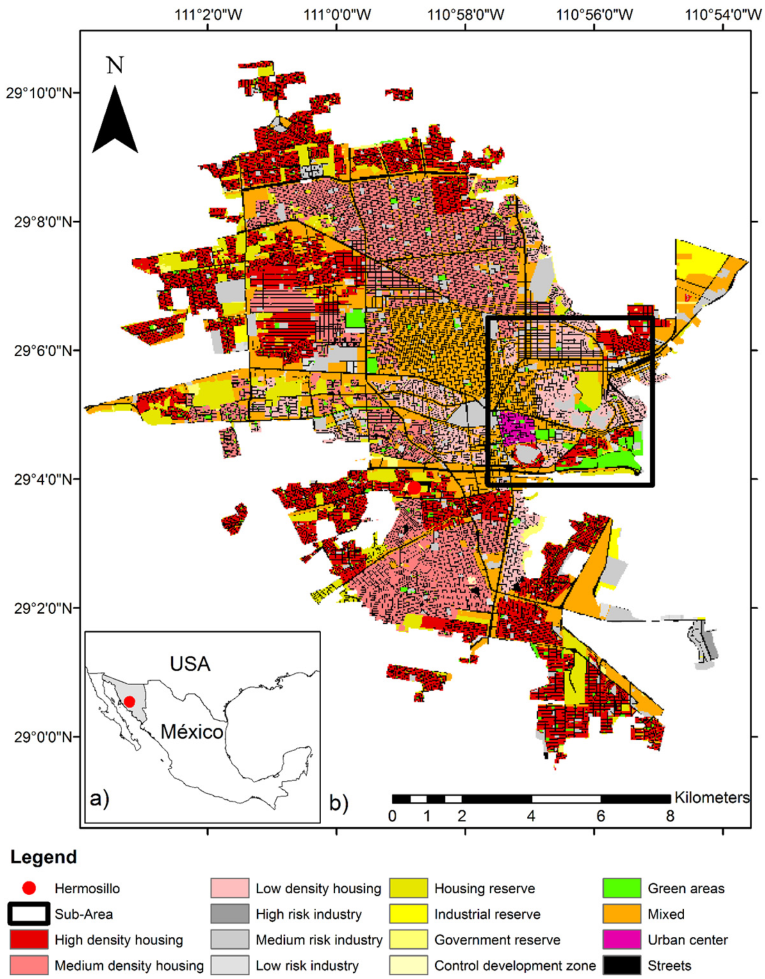

Fig. 1. (a) Location of Hermosillo in Sonora, México. (b) Official land use map (INEGI, 2015) at a 30-m resolution using the 2010 city limits. Box shows sub-area for analyses.

2. Study area

The study area is the city of Hermosillo, capital of Sonora, in northwest México (Fig. 1), with a population of 884,273 habitants (Instituto Nacional de Estadística Geografía e Informática (INEGI), 2015). The city center is located at 29°04′37″ N and 110°57′10″ W at an elevation of 211 m above sea level. Most of the city has flat terrain with a slight slope towards the southwest. According to the Köppen classification, Hermosillo has a dry desert climate with hot temperatures, BWh. Annual mean temperature is 24.9 °C, while annual maximums vary between 42 and 49.5 °C, with a positive trend of 0.03 °C/year obtained over the period of 1966 to 2016 (Navarro-Estupiñan et al., 2018). Mean annual rainfall is 356 mm/year, with 70% occurring during the summer as a result of the North American monsoon (Gebremichael et al., 2007; Tang et al., 2012).

Despite the hot, arid conditions, Hermosillo has the highest population growth rate in Sonora at 3% per year. Urban growth is regulated by the Instituto Municipal de Planeación (IMPLAN) which conducts urban land cover classifications and is responsible for providing society with information related to urban hazards, including excessive heat. Fig. 1 presents the land cover classification for the year 2014 from (Instituto Municipal de Planeación (IMPLAN), 2014), but using the city boundary for 2010 to align the efforts with the most recent census (Instituto Nacional de Estadística Geografía e Informática (INEGI), 2010). An analysis of urban land cover in Hermosillo (Table 1) reveals a high degree of built surfaces and excessively low amounts of green spaces. Indeed, a much higher percent of impervious cover (60%) is present in Hermosillo as compared to reported values in the arid cities of Phoenix (45%) and Las Vegas (40%) by (Myint et al., 2015). Furthermore, green spaces account for only 3.5 m^2 of area per inhabitant in Hermosillo, well below the (World Health Organization, 2010) recommendation of at least 9 m^2 per person to ameliorate excessive heat, among other physical, mental and wellness health goals.

Table 1
Hermosillo land use classification, including area (in km^2 and percentage), impervious cover percent in each class, and statistical properties (maximum, minimum, and mean) of *RMSE* within each class.

Code	Description	Area (km^2)	Area (%)	Imp. (%)	*RMSE*		
					Max.	Min.	Mean
H3	High density housing	23.83	14.33	75.00	0.12	0.01	0.03
H2	Medium density housing	18.70	11.25	72.00	0.12	0.01	0.03
H1	Low density housing	7.24	4.36	58.00	0.12	0.01	0.04
IRA	High risk industry	1.35	0.81	34.50	0.08	0.02	0.04
IRM	Medium risk industry	8.10	4.87	33.00	0.24	0.02	0.07
IRB	Low risk industry	0.95	0.57	34.50	0.30	0.02	0.06
RHC	Housing reserve	15.99	9.62	3.00	0.14	0.01	0.05
RIC	Industrial reserve	2.10	1.26	3.00	0.13	0.02	0.07
RG	Government reserve	2.04	1.23	3.00	0.18	0.01	0.05
ZDCS	Control development zone	0.07	0.04	7.00	0.09	0.03	0.07
AVD	Green area or sports facilities	3.10	1.87	3.00	0.17	0.01	0.04
MX	Mixed	29.99	18.04	37.00	0.26	0.01	0.04
CU	Urban center	0.47	0.28	80.00	0.08	0.02	0.03
ST	Streets	40.89	24.60	100.00	0.18	0.01	0.03

3. Data and methods

3.1. Satellite-based land surface temperature

The Thermal Infrared Sensor (TIRS) on LandSat 8 was used to obtain daytime LST over its period of availability from March 2013 to December 2017, which overlaps with the period of the urban land cover classification (year 2014). In total, 79 images were used and 31 were eliminated due to cloud cover. TIRS collects images every 16 days with an overpass time around 11:00 a.m. local time. Two thermal bands (bands 10 and 11) at 100-m resolution are used to retrieve LST but these are resampled to a finer resolution of 30-m to match the multispectral bands applied in the retrieval (Irons et al., 2012). Each image was first converted to at-sensor spectral radiance (L_λ in $Wm^{-2}sr^{-1}\mu m^{-1}$) as:

$$L_\lambda = M_L Q_{cal} + A_L, \tag{1}$$

where M_L and A_L are band-specific multiplicative and additive rescaling factors, and Q_{cal} is the quantized and calibrated standard product pixel values. L_λ was converted to at-sensor brightness temperature, T (°K), following (Zanter, 2016) as:

$$T = \frac{K_2}{\ln\left(\frac{K_1}{L_\lambda} + 1\right)} \tag{2}$$

where K_1 and K_2 are the thermal conversion constants for each band ($Wm^{-2}sr^{-1}\mu m^{-1}$). Subsequently, T was converted to LST using the procedure of (Weng et al., 2004) as:

$$LST = \frac{T}{1 + W\left(\frac{Ts}{hc}\right)\ln(e)} \tag{3}$$

where W is the wavelength of the emitted radiance, h is Planck's constant (6.626×10^{-34} Js), s is the Boltzmann constant (1.38×10^{-23} JK^{-1}), c is the velocity of light (2.998×10^8 ms^{-1}), and e is land surface emissivity obtained from the proportion of vegetation (P_v) as:

$$e = 0.004P_v + 0.986 \tag{4}$$

$$P_v = \left(\frac{NDVI - NDVI_{\min}}{NDVI_{\max} - NDVI_{\min}}\right)^2 \tag{5}$$

following (Carlson and Ripley, 1997), where *NDVI* is the Normalized Difference Vegetation Index derived from LandSat 8 (USGS, 2014), and $NDVI_{min}$ and $NDVI_{max}$ are the minimum and maximum values obtained over the study area at 30-m resolution.

3.2. Time stability analysis

Spatiotemporal variations of LST were analyzed to identify locations that behave differently than the spatially-averaged conditions in Hermosillo during the study period (i.e., hotter or colder than average). While time stability analysis has been used to characterize soil moisture variability (Vachaud et al., 1985; Jacobs et al., 2004; Vivoni et al., 2008), the methodology has not been applied to LST, to our knowledge. The procedure depends on the spatial mean of LST (LST_{mean}) for each image in the study area that was defined by the city boundary obtained from (Instituto Nacional de Estadística Geografía e Informática (INEGI), 2010) for the year

2010:

$$LST_{mean} = \frac{1}{n}\sum_{i=1}^{n} LST_i \tag{6}$$

where n is the total number of pixels and LST_i are values of each pixel i. Differences between each pixel and LST_{mean} are referred to as the Mean Relative Difference (MRD):

$$MRD = \frac{1}{m}\sum_{j=1}^{m} \frac{LST_{i,j} - LST_{mean}}{LST_{mean}} \tag{7}$$

where m is the total number of images and $LST_{i,j}$ refers to the pixel values across different times m. MRD values close to zero indicate pixels close to average conditions (LST_{mean}), while positive or negative values imply above- or below-average locations, relative to LST_{mean}. The Variance of the Relative Difference (VRD):

$$VRD = \frac{1}{m-1}\sum_{j=1}^{m} \left(\frac{LST_{i,j} - LST_{mean}}{LST_{mean}} - MRD\right)^2 \tag{8}$$

was used with MRD to obtain a single metric known as the Root Mean Squared Error of the Relative Difference ($RMSE$), (Jacobs et al., 2004) that is able to characterize time stable sites:

$$RMSE = (MRD^2 + VRD)^{0.5} \tag{9}$$

Low values of $RMSE$ indicate time stable pixels that capture spatially-averaged conditions over all time periods, while high values indicate sites that do not track the spatial mean in a consistent fashion. In prior applications, $RMSE$ has been a useful means of indicating sites that are consistently above or below the spatially-averaged conditions across all time. Here, these locations represent sites that are hotter or colder than the city averaged conditions.

3.3. Socioeconomic data analysis

Census information from (Instituto Nacional de Estadística Geografía e Informática (INEGI), 2010) at the tract (or Área Geoestadística Básica, AGEB) level was used to relate socioeconomic variables to the heat exposure map (Table 2). Five indicators linked to extreme heat deaths (gender, age, marital status, education, and health) were selected based on (Díaz-Caravantes et al., 2014), while three housing indicators were used to determine access to air conditioning, a popular heat mitigation strategy (Reid et al., 2009; Chuang and Gober, 2015). Additionally, two indicators related to infrastructure were included based on their positive relation to daytime LST, as noted by (Jenerette et al., 2016; Mathew et al., 2016). Census information was divided into five quantiles. If a particular variable belonged to the worst quantile, a value of 1 was assigned, otherwise a value of 0 was used. This worst quantile method was applied to rank and classify the vulnerability indicators in each AGEB (Smith et al., 2003). Subsequently, the ten indicators were summed and a map was obtained for the degree of heat vulnerability, classified from high (value of 10) to low (value of zero). A heat risk map was then constructed by multiplying the degree of heat vulnerability with the heat exposure obtained from the time stability analysis ($RMSE$), as suggested by (Cardona et al., 2012a; Cardona et al., 2012b). This procedure allowed creating a single heat risk map indicating unfavorable conditions from the exposure to LST and the socioeconomic vulnerability to heat hazards. A heat risk map can provide valuable information to government officials to develop heat preparedness plans and heat mitigation strategies (Loughnan et al., 2012; Hu et al., 2017).

Table 2
Selected vulnerability indicators.

Indicators by category	
ID	
	Social
1	Gender (men)
2	Age (18–65 years)
3	Marital status (single, widower or divorced)
4	Age and Education (≥ 15 years old without elementary school)
5	Health (without health public service)
Housing	
6	Without electricity
7	Without fridge and washing machine
8	Without internet access, phone and cellphone
Infrastructure	
9	Impervious area
10	Streets

3.4. Hot spot analysis

The "hot spot" term is defined as a region whose value is higher relative to its surroundings (Isobe et al., 2015). The Getis-Ord local clustering method was applied to find statistically significant "hot" and "cold" spots in the heat risk map (Getis and Ord, 1992). G_i* is a Z-score, with large values implying a more intense clustering of high values:

$$G_i{}^*(d) = \frac{\sum_{j=1}^{n} W_{ij}(d)x_j}{\sum_{j=1}^{n} x_j} \tag{10}$$

where $G_i{}^*$ (d) is the local G statistic for a feature i within a distance (d), and W_{ij} (d) is the spatial weight for the target-neighbor i and j pair (Peeters et al., 2015). (Ord and Getis, 1995) developed a z-transformed form of Gi^* to improve the statistical testing. The statistical significance and degree of clustering is evaluated according to the confidence level and on the Z-scores. If $Z(G_i{}^*)$ has a positive value and significant, it means that the pixel has a relatively high frequency of being a hot spot area. Otherwise, if $Z(G_i{}^*)$ has a negative value and significant, the pixel has a high frequency of being a cold spot area.

4. Results and discussion

4.1. Spatiotemporal variations of LST and NDVI

Prior to conducting spatiotemporal analyses, we compared LST values obtained from LandSat 8 with observed air temperatures over the study period. While indirect, this comparison provides a context for the retrieval performance relative to other studies. A single weather station located in the center of the urban area (29.0814°N, 110.9706°W) was available for this comparison ("Hermosillo Observatorio"). We found a strong linear correlation ($y = 0.9453\times\ + 6.5851$, $r = 0.74$) between LST and air temperature at the LandSat 8 local passing time (11:00 a.m.). The correlation at this site could be affected by atmospheric turbulence since the weather station is installed on the roof of a three-story building. Furthermore, the relation is expected to vary across different types of urban land cover, depending on urban geometry, built environment material properties, and outdoor water use (Templeton et al., 2018; Song et al., 2017). Despite these factors, the comparison at "Hermosillo Observatorio" is similar to comparisons reported by (García-Cueto et al., 2007; Jenerette et al., 2011) in the arid cities of Mexicali and Phoenix, respectively.

To provide context for the study period, Fig. 2 shows the temporal variations of LST (°C) and NDVI (−) obtained from LandSat 8, along with daily rainfall (mm/day) from the "Hermosillo Observatorio". In the case of the LST and NDVI, the spatial average in the city of Hermosillo for the 2010 boundary is shown as a symbol, with the variations in the city captured by bars representing ± 1 spatial standard deviation. Higher values of NDVI and rainfall tend to occur during the summer (July to September) associated with the North American monsoon (Xiang et al., 2014). This period is also characterized by a reduction of LST, as compared to the spring season and early summer (May to June), due to evaporative cooling (Berg et al., 2015). As a result, an analysis of the correlation between NDVI and LST yielded slight negative correlations ($r = -0.10$), which were statistically significant ($p < 0.001$). Moreover, LST exhibited sensitivity to rainfall ($r = -0.02$) in agreement with (Haashemi et al., 2016). Although the correlation is not statistically significant, there is an average LST reduction of 5.78 °C compared to the previous day without precipitation. Note that high LST in early summer presents the most hazards to health in Hermosillo, but that the onset of summer rains can effectively reduce these risks.

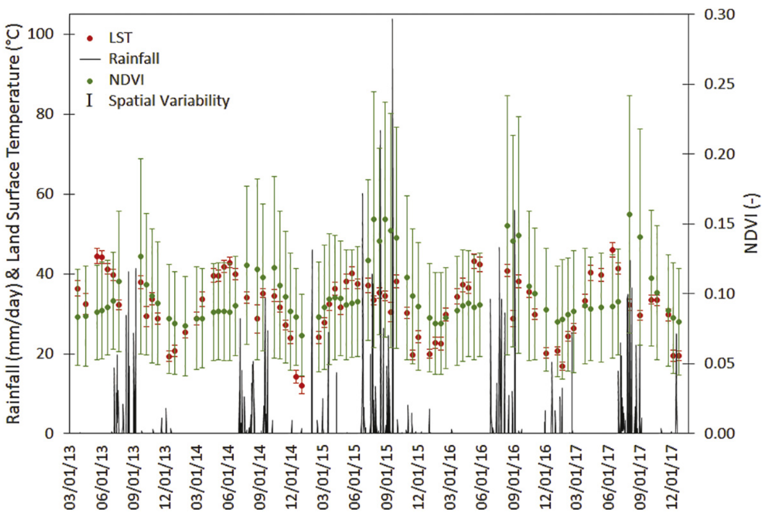

Fig. 2. Temporal variations of spatially-averaged LST and NDVI over Hermosillo (symbols) and its variation (error bars are ± 1 standard deviation) with rainfall obtained from the weather station "Hermosillo Observatorio" during the study period.

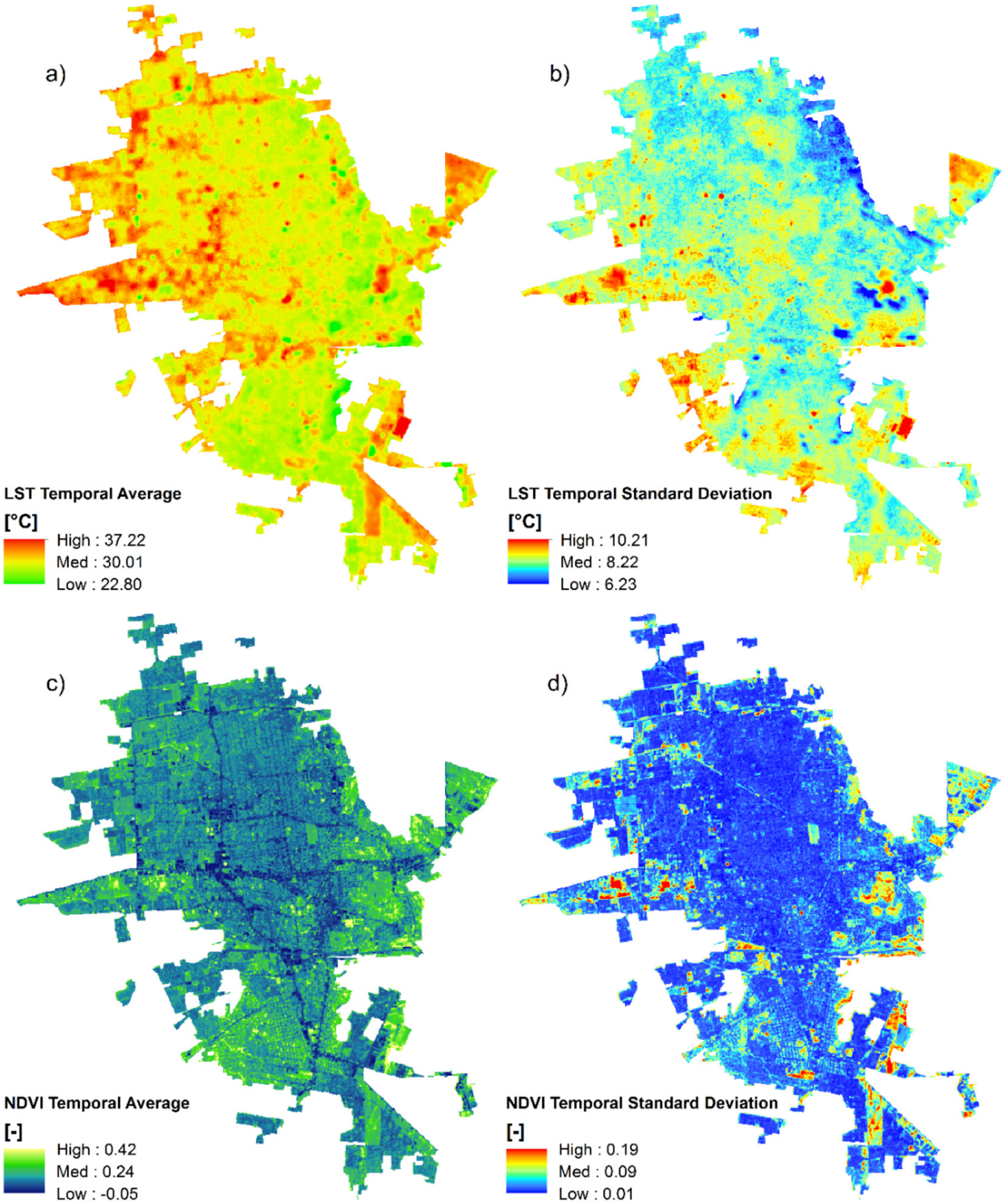

Fig. 3. Spatial distributions of LST and NDVI statistics obtained during the study period: temporal average (a) and temporal standard deviation (b) of LST, and temporal average (c) and temporal standard deviation (d) of NDVI.

Fig. 3 presents the spatial distribution of the temporal averages and standard deviations of LST and NDVI, obtained at 100-m and 30-m resolution over all available image dates, respectively. Note that there are areas in Hermosillo characterized by higher LST towards the city periphery, especially along the eastern and western areas. In contrast, central areas in the city have lower LST values. This effect has been reported in other desert cities (Lazzarini et al., 2015; Hafner and Kidder, 1999). This can be explained considering that impervious surfaces tend to respond more slowly to temperature changes in the morning than the desert surroundings (Steeneveld et al., 2011). In addition, shaded areas produced by buildings leads to LST reductions (Tang et al., 2017). Regions with high LST tend to experience large temporal changes in LST, whereas cooler areas have lower variability. Spatial differences in NDVI are also noted, with higher values associated with peripheral areas, urban green spaces and agriculture (especially in the southwest area). In contrast, streets and mixed to high density urban areas show a clear reduction in NDVI. As expected, the temporal variations in NDVI are lower than those of LST, with only those areas having changes in land cover exhibiting appreciable standard deviations. One of the many factors explaining the spatial variations in temporal average LST and NDVI are elevation differences, notably due to

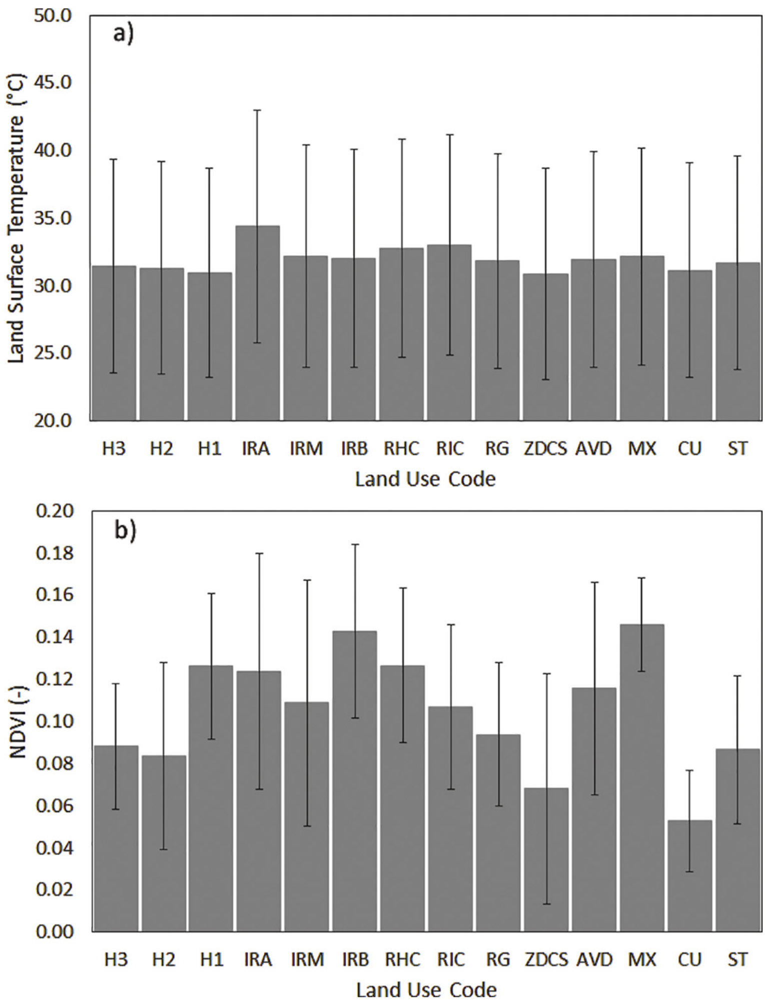

Fig. 4. Average (bars) and ± 1 standard deviation (error bars) of (a) LST and (b) NDVI within each land use type during the study period (see Table 1 for code definitions).

small mountains found in the northern and central areas of the city. We found that LST decreases with elevation ($r = -0.19$ and $p < 0.001$), while NDVI increases slightly with altitude ($r = 0.03$ and $p < 0.001$). In addition, the land cover type is expected to control LST and NDVI, as explored next.

4.2. Effects of urban land cover type

Fig. 4 presents the variation of LST and NDVI with the urban land cover types (see Table 1). Each bar depicts the averaged conditions across all pixels classified in the particular type over the study period, while the error bars depict the ± 1 standard deviation among these pixels over all images. In terms of LST, industrial areas (IRA) exhibited the highest average, which were substantially greater than those across all other types. This is in agreement with (Alpuche et al., 2014) who found industrial areas in Baltimore to exhibit the highest LST values. Small differences in LST between different housing densities are likely due to lower amounts of NDVI for the medium and high density areas. It is worth noting that high density housing (H3) has increased more rapidly in the last decade in Hermosillo (Hernández and Velásquez, 2014; Mathew et al., 2017). Unexpectedly, green areas or sports facilities (AVD) were found to exhibit similar LST to housing types, due to the barren conditions and low use of irrigation to support vegetation. It is well known that vegetated areas with high NDVI can help reduce extreme heat (Kroeger et al., 2018; Liu and Zhang, 2011). This is found in Hermosillo by comparing the LST and NDVI for the urban land cover types. For housings (H1, H2, H3) and reserves (RHC, RIC, RG), a negative correlation ($r = -0.21$ and $p < 0.001$) was obtained between LST and NDVI such that vegetation in these areas reduced land surface temperatures. In contrast, we found a positive correlation among LST and NDVI for industrial areas (IRA, IRM, IRB; $r = 0.34$ and $p < 0.001$) and mixed areas (MX; $r = 0.22$ and $p < 0.001$). This indicates that elements of the built environment and construction materials increase LST despite the occurrence of high NDVI (Jenerette et al., 2016; Harlan et al., 2014). However, the lowest NDVI values were obtained in the urban center (CU) with the high percentage of impervious

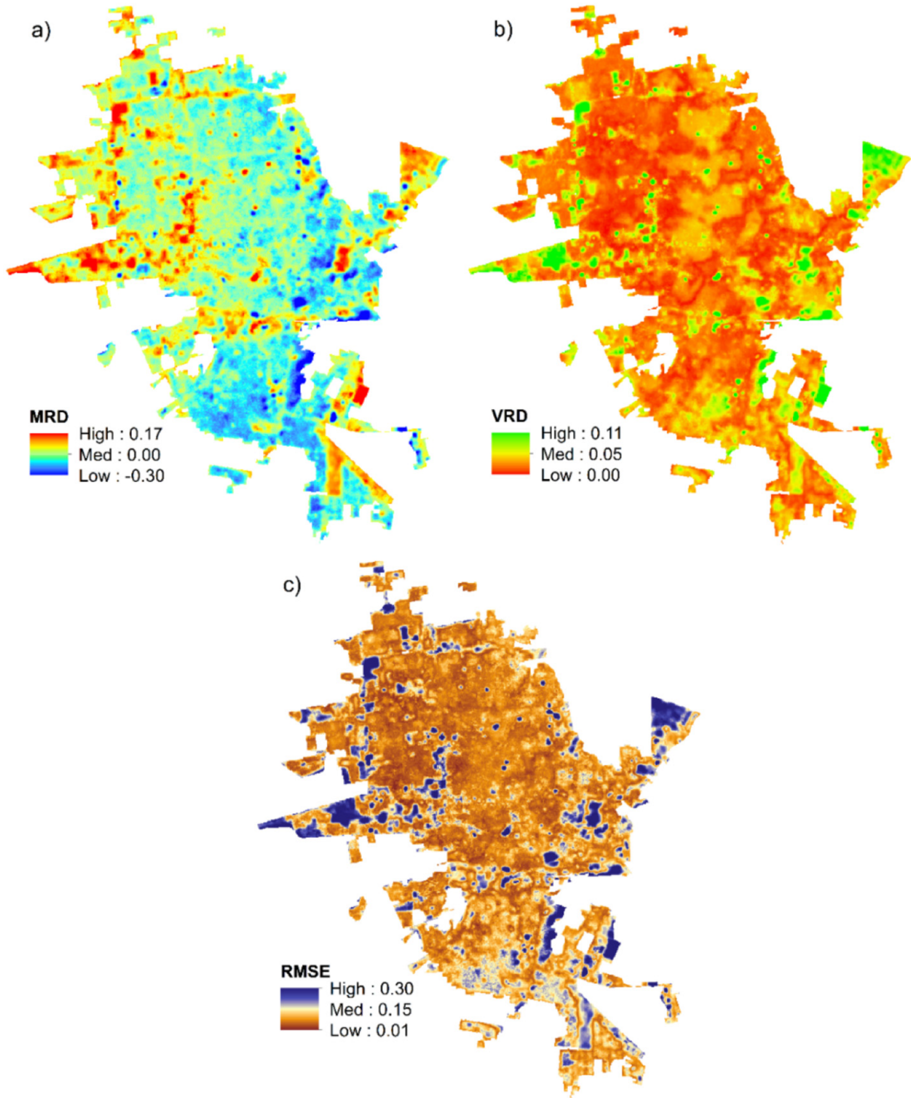

Fig. 5. Spatial distributions of (a) mean relative difference (*MRD*), (b) variance of the relative difference (*VRD*) and (c) root mean square error of the relative difference (*RMSE*) of land surface temperature during the study period.

surfaces and where vegetation is absent. Clearly, there are factors other than NDVI that help to control the LST patterns across the multitude of urban land cover types in Hermosillo. Next, we explore which areas have consistently warmer or cooler LST values.

4.3. Time stability analysis of land surface temperature

Fig. 5 presents the outcomes of the time stability analysis for LST variations in Hermosillo. We selected the 2010 city boundary as the domain to calculate LST_{mean} (as shown in Fig. 2 as a time series) as this was the most recent census data available. It is expected that land cover changes occurred during the study period (2013–2017) such that the classifications of 2014 would be altered. These changes, for instance in terms of urban expansion or crop rotations, would have an impact on LST that are reflected in the time stability analysis. Note that we present spatial distributions of the two factors of the analysis, *MRD* and *VRD*, that together form the *RMSE* metric. Recall that *MRD* values close to zero are those pixels that track LST_{mean}, while positive or negative values are above or below the spatial average. Fig. 5a illustrates spatial clustering of *MRD* in an identical pattern as LST_{mean} (Fig. 3a), with large portions of the city having values close to zero. As described earlier, the city center has areas with negative *MRD* (cooler than average), while areas in the city periphery linked to fallow agriculture or undeveloped land have positive *MRD* (warmer than average). In contrast, *VRD* values show spatial clustering which are not identical to the standard deviation of LST (Fig. 3b), but instead reflect whether a location changes in its relation to the spatial average conditions (larger *VRD*) or remains similar over time (smaller *VRD*). Those areas in the city periphery with positive *MRD* also exhibit high *VRD*, indicating that they experienced changes over time, possibly linked to

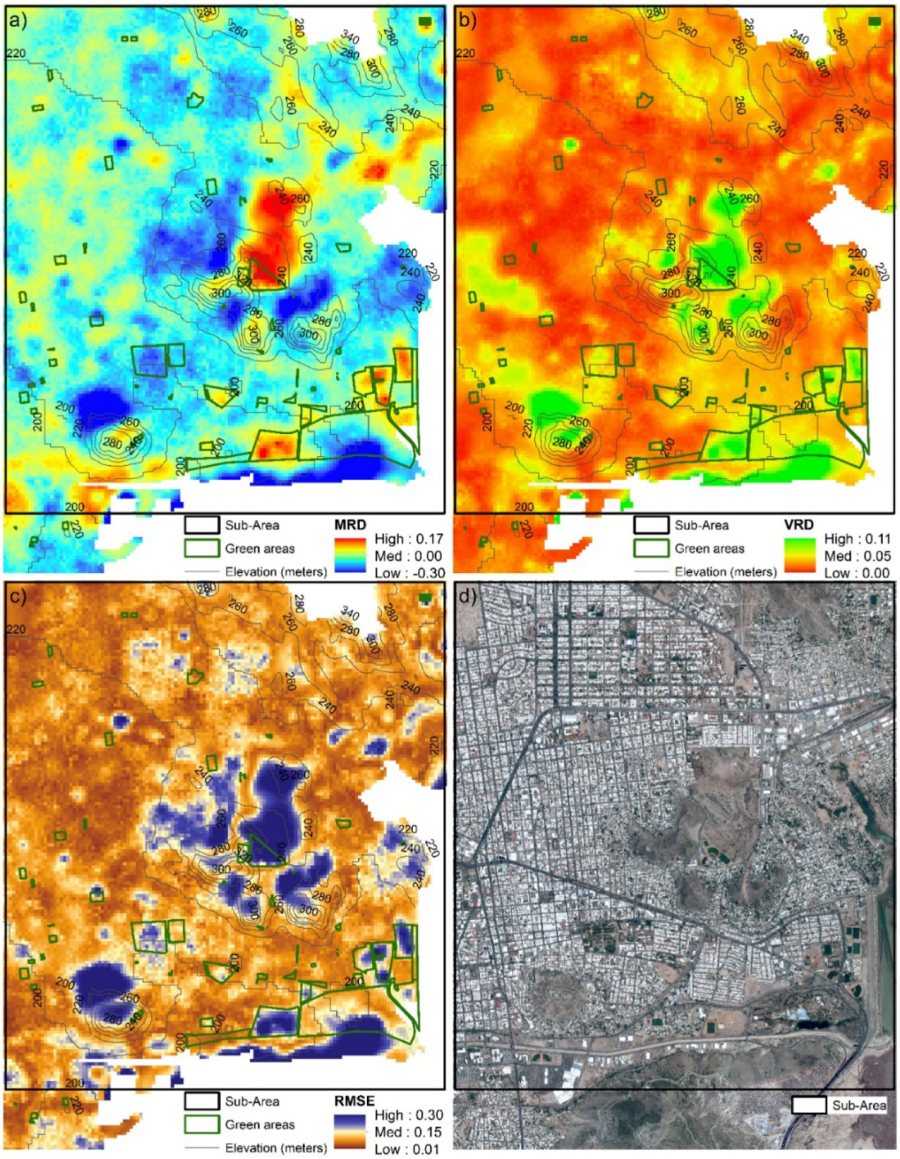

Fig. 6. As in Fig. 5, but for sub-area depicted in Fig. 1.

alterations in land cover. The city center exhibits small values of *VRD* in part due to its stable land cover over the study period, but also as a reflection of tracking well the spatial average.

As an integrated measure, *RMSE* is useful for interpreting the spatial patterns of LST, as shown in Fig. 5c, and computed for urban land cover types in Table 1 (minimum, maximum and mean values for all pixels in each classification). Low *RMSE* values indicate areas with time stable pixels, defined as those areas that track well the spatially-averaged conditions in Hermosillo over all time. These pixels are located mainly in land use types such as residential housing, urban centers, streets, mixed uses and green areas (Table 1, $RMSE \leq 0.04$). High *RMSE* values are those sites that do not track well the spatially-averaged conditions in Hermosillo over time, either due to variations in magnitude (as indicated by *MRD*) or in temporal changes (as indicated by *VRD*). It is important to note that high *RMSE* does not implicate a particular directionality of LST such that these areas can be warmer or cooler than overall conditions in the city. At the scale of the city, Fig. 5c and Table 1 show that industrial zones and reserve areas in the periphery of the city exhibit high *RMSE* (Table 1, $RMSE \geq 0.05$). Nevertheless, other patterns emerge in *RMSE* that are unaffected directly by land cover type. For instance, a significant, but small correlation ($r = 0.01$, $p < 0.001$) was found between *RMSE* and elevation, suggesting that higher altitude areas have a higher *RMSE*.

Fig. 6 provides additional information on this effect by showing details in the sub-area box depicted in Fig. 1 in terms of *MRD*, *VRD*, and *RMSE*. Note that large areas with high *RMSE* tend to be associated with higher elevation zones and urban parks that are irrigated. The elevation effect is two-fold in that: (1) higher altitude provide refugia to heat and thus do not track well the overall

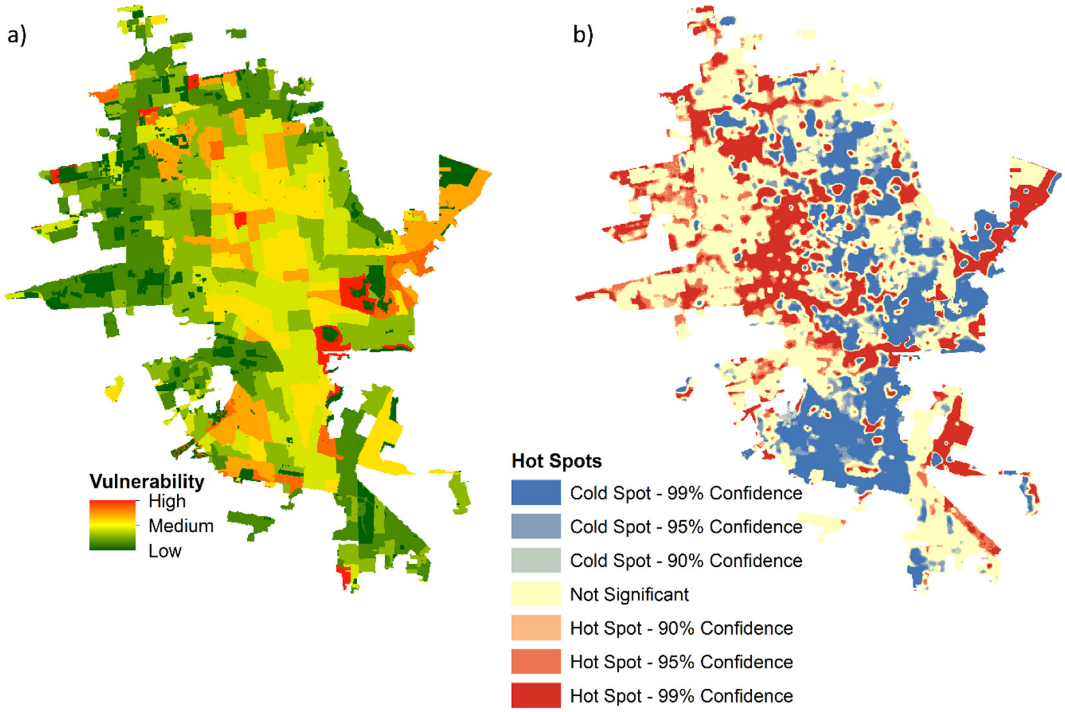

Fig. 7. Spatial distributions of (a) vulnerability map from the worst quantile method of the socioeconomic indicators and (b) hot and cold spot areas with 99%, 95% and 90% confidence that combine vulnerability to heat and exposure to heat through *RMSE*.

conditions in the city, and (2) small mountains in Hermosillo provide substantial shading to nearby areas, in particular to locations northeast of each mountain. Some small urban parks, however, are not effective in significantly changing the conditions as compared to the overall city, likely due to the lack of outdoor water use to support vegetation and the abundant use of synthetic grass. Thus, several factors affect exposure to heat, as compared to the averaged conditions in the city, which will be combined next with the vulnerability to heat to identify areas of heat risks.

4.4. Vulnerability and heat risk mapping

The worst quantile method was used to spatially characterize the ten socioeconomic variables and create a vulnerability map as shown in Fig. 7a. We also excluded areas that are uninhabited such as housing, industrial and government reserves and those sites with known development restrictions. Zones of high vulnerability were identified near the city center associated with CU, H1, H3, and MX urban land cover classes (see Table 3). Some areas within the city center that are classified as low vulnerability are occupied by government offices or designated as uninhabited. A large area of medium to high vulnerability extends from the north to the south

Table 3
Vulnerability and hot/cold spot analysis using the 2010 city boundary. Metrics include the average vulnerability score (0 is low and 10 is high vulnerability) and the percentage of area that is classified as a cold or hot spot above the 99% confidence interval.

Code	Description	Vulnerability	Cold spot > 99% (%)	Hot spot > 99% (%)
H3	High density housing	2.22	14.68	7.65
H2	Medium density housing	3.10	37.06	9.45
H1	Low density housing	3.16	39.84	3.97
IRA	High risk industry	2.07	0.00	56.18
IRM	Medium risk industry	3.03	15.96	58.69
IRB	Low risk industry	3.11	19.98	51.06
RHC	Housing reserve	2.31	3.49	5.82
RIC	Industrial reserve	3.24	0.07	3.15
RG	Government reserve	3.23	4.14	11.42
ZDCS	Control development zone	3.00	3.13	0.00
AVD	Green area or sports facilities	2.82	13.63	36.15
MX	Mixed	3.07	14.76	36.16
CU	Urban center	4.16	65.26	1.92
ST	Streets	2.83	20.85	16.77

of the city where there are mainly H1, H2 and MX urban classes. Towards the periphery of the city in northern, western and southern areas, large swaths of low vulnerability zones are present which are related to H2, H3, MX, and RHC urban classes. Thus, there are regions in the periphery that despite having dense urban housing are classified as having low vulnerability based on the evaluated indicators (Table 2). Overall, the percentages of population of Hermosillo in 2010 can be classified as living in high (16.6%), medium (13.9%) and low (70.4%) vulnerability zones.

Fig. 7b presents the heat risk map derived for Hermosillo based on the vulnerability indicators and the *RMSE* in the form of the distribution of hot spots and cold spots with 90%, 95% and 99% confidence intervals, as well as non-significant areas. To aid in the interpretation, Table 3 summarizes the percentage of area of each urban land cover type that is classified as a hot and cold spot at the 99% confidence interval. The largest hot spot areas are located in the older neighborhoods of the city located in the eastern and central areas, as well as in recent and high density housing developments in the north and south. Overall, hot spots account for 20.5% of the area for the city boundary of 2010. These hot spots occupy large areal fractions of the medium risk industry and mixed use areas (Table 3). Those classes categorized as housing (H1, H2, H3, CU, and MX) have significant hot spots occupying from 10 to 24% of the total area. Hot spots indicate areas where mitigation strategies such as the implementation of green infrastructure could reduce the level of heat exposure and where prevention campaigns could be targeted. In contrast, cold spots are located in the periphery of the city where vulnerability to heat tend to be low, accounting for 42.0% of the total area in Hermosillo. Some contrasts between hot and cold spots are worth noting from Table 3. For instance, green area or sports facilities (AVD) and high density housing (H3) have two to five times more cold spots as compared to hot spots, while significantly more area in the urban center is a hot spot as compared to a cold spot.

A closer look at the sub-area box near the urban center is shown in Fig. 8 to illustrate the spatial distribution of vulnerability and hot and cold spots relative to a high-resolution image. A few old neighborhoods at the lower end of the income scale in Hermosillo exhibit high vulnerability and are hot spots. These are found next to small mountains that have a low vulnerability and are generally not significant spots. Medium vulnerability is also found in housing areas in the urban center, where these fall within the insignificant areas of the hot spot analysis. Interestingly, there seems to be little correlation between the location of green areas designated by the city and the occurrence of hot or cold spots, except some sites in the southern part of the sub-area where irrigated parks are cold spots, suggesting the utility of green infrastructure to mitigate heat in Hermosillo.

Note that mortality was not included as one of the social variables of the analysis because it is reported at the city scale by the epidemiology office of the state. Social exclusion is a condition related to excessive mortality. Hence, it is possible that a synergistic effect between thermal vulnerability and frailty occurs.

4.5. Sensitivity analyses

To understand the sensitivity of the heat risk map to the underlying assumptions in the adopted methods, we performed two different types of analyses. In the first approach, the sensitivity to each of the socioeconomic variables was assessed by withholding one indicator at a time from the evaluation. The socioeconomic variables only dictate the vulnerability to heat and propagate to the heat risk map without affecting the estimation of *RMSE*. As a sensitivity metric, we determined the differences in hot spot areas as compared to that obtained with the analysis of all indicators. The most sensitive indicators were found to be “Age and Education (> = 15 years old without elementary school)” with a 2.0% difference in hot spot area, followed by “Health (without health public service)” at 1.6% difference and “Age (18-65 years)” at 1.1% difference. These indicators are related to heat exposure through outdoor activities such labor in construction and agricultural activities, consistent with the findings of Harlan et al. (2014), and provide guidance as to potential heat mitigation efforts aimed at populations with these characteristics. Overall, however, the sensitivity to any individual indicator was low, indicating the robustness of the overall heat risk map to the particular selection of individual socioeconomic factors.

In the second approach, we determined the sensitivity of the heat risk map to the selection of the city boundary polygon. Note the city area is a critical factor for determining the *RMSE* from LST imagery as all locations are referenced to spatial average, LST_{mean}. This was performed by using the official city polygons over different periods spanning from 1950 to 2010 (Instituto Municipal de Planeación (IMPLAN), 2014). Fig. 9 (inset) shows an expansion of about 13-fold in the Hermosillo area over this period, with the largest increase from 1990 to 2000, and the change in LST_{mean} with the size of the city boundary. Accompanying this expansion were significant modifications in land cover which affected the occurrence of urban classes. For example, Table 4 presents the vulnerability and areal percentage of cold (> 99%) and hot (> 99%) spots for the 1950 city polygon concentrated around the urban center (within the sub-area box of Fig. 1). Using the 1950 polygon, the CU land cover class has only 2.33% of its area as a hot spot, as compared to 15.76% for the 2010 polygon. This indicates that the smaller area for spatially-averaging decreases LST_{mean} (Fig. 9 inset) and that deviations from this quantity are less common in the CU class for the 1950 case. Similarly, for the green areas and sports facilities (AVD), the use of the 1950 polygon leads to a smaller percentage of cold spots (20.69%) as compared to the 2010 polygon (28.23%). The vulnerability of CU and AVD remained fairly similar since these classes have a large presence near the city center included in the 1950 polygon. Thus, in contrast to the low sensitivity found for socioeconomic indicators, we identify that the selection of the averaging area is a critical step in determining a heat risk map using this method.

Since the area of the city has not varied significantly since 2000 (Fig. 9 inset), we conclude that the results of the heat risk mapping are generally valid over the period 2000 to 2017. Note that the results of the sensitivity analysis do not imply that we have captured the temporal variation of heat risk between 1950 and 2010. Instead, this should be viewed as the sensitivity of the heat risk map to the spatial averaging of the LST imagery obtained from LandSat 8 (2013–2017). As the boundary polygon grows, the distributions of cold and hot spots change, in accordance with the new estimate of LST_{mean} (Fig. 9 inset). The growth of the polygon

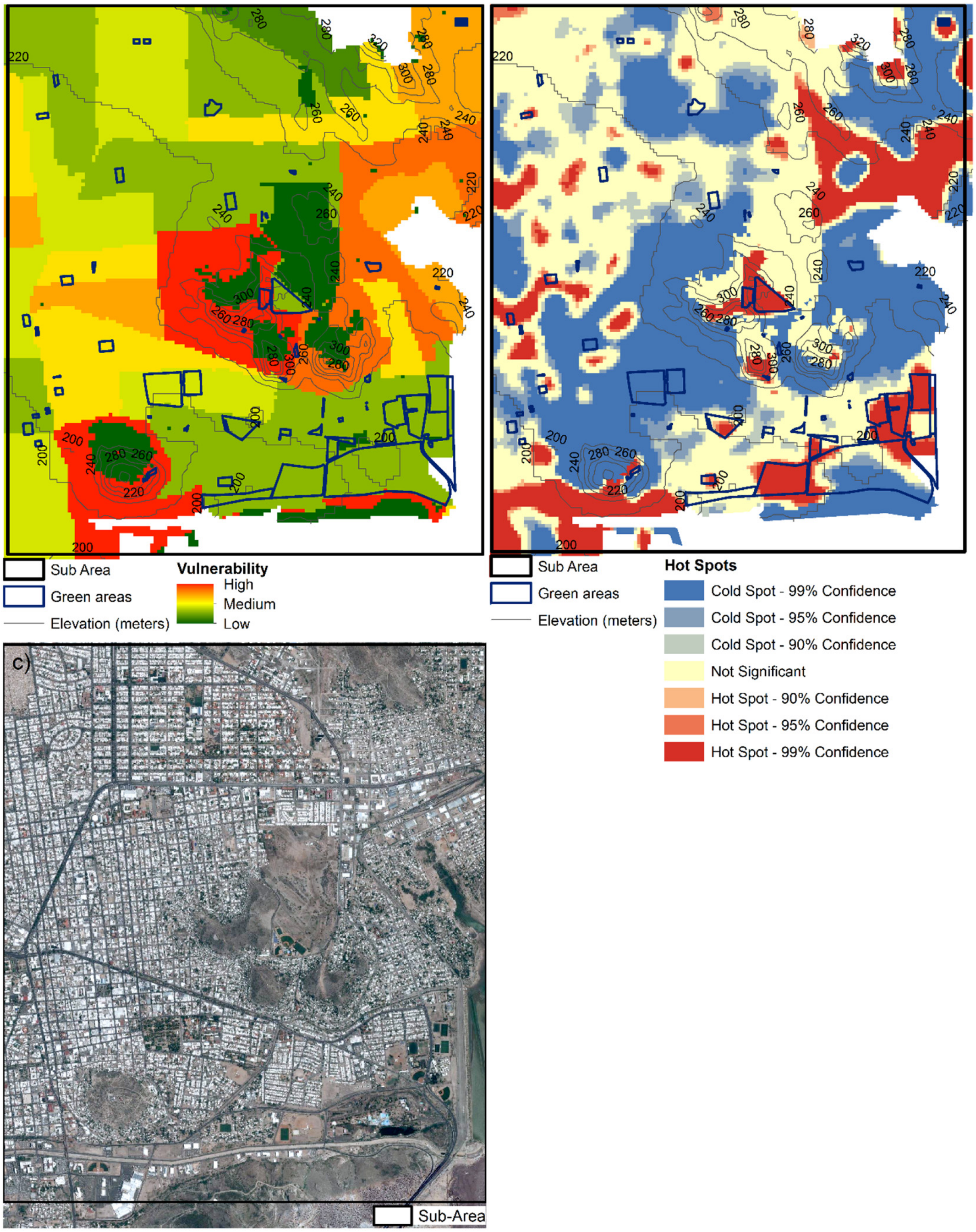

Fig. 8. As in Fig. 7, but for sub-area depicted in Fig. 1.

incorporates hotter regions along the periphery of the city, thus leading to a rising LST_{mean}. This is illustrated in Fig. 9 using two examples: (1) cold spot area percentage within the green areas and sports facilities (AVD), and (2) hot spot area percentage within the urban center (CU). As the boundary polygon grows, the AVD class is a smaller percentage of the total area and its percentage of cold spots decreases from 1950 to 1970. The cold spots then increase from 1980 to 2010 despite the LST_{mean} rising. Overall, this implies that the effect of green areas in ameliorating urban heat is more effective as more of the city area is considered. This is contrasted by the gradual increase in the hot spot area percentage within the CU urban class located near the historical center. As the city polygon grows, CU becomes a much smaller percentage of the total area, which is experiencing an increase in LST_{mean}. A growth in the hot spot percentage within CU, despite the rising LST_{mean}, indicates that those areas added over time have sufficient variability in LST such that the high density urban center effectively has comparatively higher heat risk.

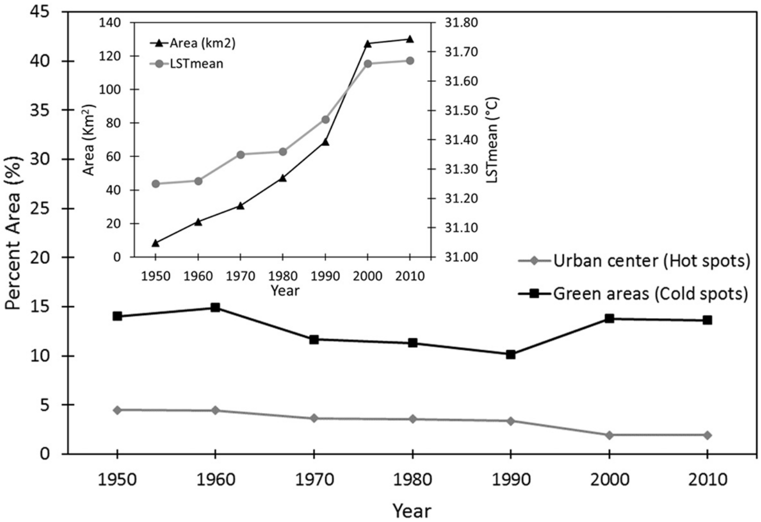

Fig. 9. Variation of urban center classified as a hot spot and green areas classified as a cold spot above the 99% confidence interval based on city polygons defined from 1950 to 2010. Inset shows the total area of the city (km^2) and LST_{mean} (°C) as a function of the city polygons defined from 1950 to 2010. (For interpretation of the references to colour in this figure legend, the reader is referred to the web version of this article.)

Table 4
As Table 3, but using the 1950 city boundary.

Code	Description	Vulnerabilty	Cold spot > 99% (%)	Hot spot > 99% (%)
H3	High density housing	4.25	22.68	7.03
H2	Medium density housing	3.00	0.00	0.00
H1	Low density housing	4.06	32.28	1.92
IRA	High risk industry	0.00	0.00	0.00
IRM	Medium risk industry	0.00	0.00	0.00
IRB	Low risk industry	2.00	0.00	0.00
RHC	Housing reserve	2.00	0.00	0.00
RIC	Industrial reserve	0.00	0.00	0.00
RG	Government reserve	1.00	0.00	33.33
ZDCS	Control development zone	0.00	0.00	0.00
AVD	Green area or sports facilities	3.02	14.01	11.67
MX	Mixed	3.86	8.60	22.13
CU	Urban center	3.89	17.76	4.49
ST	Streets	4.01	13.48	19.15

5. Conclusions

The city of Hermosillo has the second highest number of mortalities linked to heat in México (Díaz-Caravantes et al., 2014). However, there are no current studies to link the spatial distribution of exposure to heat and the socioeconomic vulnerability to heat in the population. In this study, we develop the first heat rissk map for Hermosillo by combining land surface temperature imagery from satellite remote sensing with census data using two techniques, namely time stability and hot spot analyses. The methods are generalizable to other cities confronting heat hazards, for instance Phoenix, Arizona (Chow et al., 2012) or Mexicali, Baja California (García-Cueto et al., 2007), based on available government records and thermal remote sensing datasets. Furthermore, the resulting heat risk map is a useful tool for urban planners in the city of Hermosillo who have responsibilities linked to emergency preparedness during heat waves and infrastructure planning to ameliorate urban heat. Indeed, interactions with IMPLAN have yielded a strong interest in using the heat risk map (G. Peñuñurí, personal communication). Results from this study reveal:

(1) Substantial spatial variability is present in LST within the city of Hermosillo, but a few factors, including NDVI, elevation and urban land cover type, help to explain the identified patterns. The temporal variability of LST is dictated in large part by the lack of or occurrence of rainfall prior to and during the North American monsoon. We found contrasting relationships between NDVI and LST depending on the urban land cover type. We also some unexpected outcomes such as a high LST in green areas and sports facilities, comparable to housing areas, since these are not irrigated to support vegetation.
(2) Through the time stability analysis, we identified locations in Hermosillo with high *RMSE* that exhibit above- or below-average LST conditions relative to the overall city. Large areas with high *RMSE* tend to be associated with industrial zones, reserve areas in the periphery of the city, higher elevation zones, and urban parks that are irrigated, whereas other land cover types tend to

follow the spatially-averaged conditions in the city well (low *RMSE*). Local conditions such as shadowing effects from nearby mountains or outdoor water use can play important roles in determining urban heat in Hermosillo.

(3) Heat exposure maps obtained from *RMSE* were combined with socioeconomic indicators of vulnerability to heat to derive hot and cold spots within the city. This planning tool can be used to identify locations where heat mitigation strategies (hot spots) would yield important benefits or sites that already serve as heat refugia (cold spots). We tested the sensitivity of the selection of the socioeconomic indicators finding that the outcomes were robust. Nevertheless, the heat risk map was identified as sensitive to the city polygon used as the averaging domain, though the current map appears valid from 2000 to 2017.

While this study is based on LandSat 8 TIRS imagery over a limited period of availability (2013–2017), the results obtained here are considered to be robust for emergency preparedness and infrastructure planning activities in Hermosillo. Indeed, earlier versions of the work have been used directly by IMPLAN to inform citizens of Hermosillo, through local news media and web resources, about areas to avoid during summer heat waves (C. Espinoza, personal communication). The methodology presented in this work is readily adapted to novel sources of high-resolution LST imagery; to other arid and semiarid cities in Mexico and the United States; and as a basis for decision support systems that combine heat risks with other measures of environmental vulnerability. In particular, the heat risk map affords the opportunity for targeted investments and/or activities that can have a large impact on reducing heat-related health issues and mortality.

Acknowledgements

We acknowledge the support of CONACYT for J.N.E. through a graduate fellowship. This material was supported by the Urban Resilience to Extreme Events Sustainability Research Network of the National Science Foundation under award number: SES-1444755. We would also like to thank ITSON's Programa de Fomento y Apoyo a Proyectos de Investigacion (PROFAPI) for funding provided for this study. We acknowledge Carolina Espinoza and Eduardo Robles-Hinojosa from IMPLAN and Jaime Garatuza-Payan and Vivian Verduzco from ITSON for help in obtaining datasets. LandSat 8 data can be obtained at http://earthexplorer.usgs.gov, while data from Hermosillo are available at http://www.implanhermosillo.gob.mx/ and http://sustainability.asu.edu/urbanresilience/collaboration.

References

Aina, Y., Adam, E., Ahmed, F., 2017. Spatiotemporal variations in the impacts of urban land use types on urban heat island effects: the case of Riyadh, Saudi Arabia. In: 37th International Symposium on Remote Sensing of Environment, pp. 9–14.

Alpuche, M.G., González, I., Ochoa, J.M., Marincic, I., Duarte, A., Valdenebro, E., 2014. Influence of absorptance in the building envelope of affordable housing in warm dry climate. Energy Procedia 57, 1842–1850.

Arnfield, A.J., 2003. Two decades of urban climate research: a review of turbulence, exchanges of energy and water, and the urban heat island. Int. J. Climatol. 23 (1), 1–26.

Azevedo, J.A., Chapman, L., Muller, C.L., 2016. Quantifying the daytime and night-time urban heat island in Birmingham, UK: a comparison of satellite derived land surface temperature and high resolution air temperature observations. Remote Sens. 8 (2), 1–17.

Berg, A., Lintner, B.R., Findell, K., Seneviratne, S.I., van den Hurk, B., Ducharne, A., Chéruy, F., Hagemann, S., Lawrence, D.M., Malyshev, S., Meier, A., Gentine, P., 2015. Interannual coupling between summertime surface temperature and precipitation over land: processes and implications for climate change. J. Clim. 28 (3), 1308–1328.

Cardona, O., van Aalst, M., Birkmann, J., Fordham, M., McGregor, Mechler, R., Field, C.B., Barros, V., Stocker, T.F., Qin, D., Dokken, D., Ebi, K., Mastrandrea, M.D., Mach, K.J., Plattner, G.-K., Allen, S.K., Tignor, M., Midgley, P.M., 2012a. Determinants of risk: exposure and vulnerability. In: Managing the Risks of Extreme Events and Disasters to Advance Climate Change Adaptation. Cambridge University Press, Cambridge, UK, and New York, NY, USA, pp. 65–108.

Cardona, O., van Aalst, M., Birkmann, J., Fordham, M., McGregor, Mechler, R., Field, C.B., Barros, V., Stocker, T.F., Qin, D., Dokken, D., Ebi, K., Mastrandrea, M.D., Mach, K.J., Plattner, G.-K., Allen, S.K., Tignor, M., Midgley, P.M., 2012b. Determinants of risk: exposure and vulnerability. In: Managing the Risks of Extreme Events and Disasters to Advance Climate Change Adaptation. Cambridge University Press, Cambridge, UK, and New York, NY, USA, pp. 65–108.

Carlson, T.N., Ripley, D.A., 1997. On the relation between NDVI, fractional vegetation cover, and leaf area index. Remote Sens. Environ. 62, 241–252.

Chen, X.L., Zhao, H.M., Li, P.X., Yin, Z.Y., 2006. Remote sensing image-based analysis of the relationship between urban heat island and land use/cover changes. Remote Sens. Environ. 104 (2), 133–146.

Chow, W.T., Brennan, D., Brazel, A.J., 2012. Urban heat island research in Phoenix, Arizona: theoretical contributions and policy applications. Bull. Am. Meteorol. Soc. 93 (4), 517–530.

Chow, W.T., Volo, T.J., Vivoni, E.R., Jenerette, G.D., Ruddell, B.L., 2014. Seasonal dynamics of a suburban energy balance in Phoenix, Arizona. Int. J. Climatol. 34 (15), 3863–3880.

Chuang, W.G., Gober, P., 2015. Predicting hospitalization for heat-related illness at the census-tract level: Accuracy of a generic heat vulnerability index in Phoenix, Arizona (USA). Environ. Health Perspect. 123 (6), 606–612.

Cui, Y.Y., De Foy, B., 2012. Seasonal variations of the urban heat island at the surface and the near-surface and reductions due to urban vegetation in Mexico City. J. Appl. Meteorol. Climatol. 51 (5), 855–868.

De Faria Peres, L., de Lucena, A.J., Rotunno Filho, O.C., de Almeida França, J.R., 2018. The urban heat island in Rio de Janeiro, Brazil, in the last 30 years using remote sensing data. Int. J. Appl. Earth Obs. Geoinf. 64, 104–116.

Díaz-Caravantes, R.E., Castro-Luque, A.L., Aranda-Gallegos, P., 2014. Mortalidad por calor natural excesivo en el noroeste de México: Condicionantes sociales asociados a esta causa de muerte. Front. Norte 26 (52), 155–177.

García-Cueto, O.R., Jauregui-Ostos, E., Toudert, D., Tejeda-Martinez, A., 2007. Detection of the urban heat island in Mexicali, BC, México and its relationship with land use. Atmósfera 20 (2), 111–131.

Gebremichael, M., Vivoni, E.R., Watts, C.J., Rodríguez, J.C., 2007. Submesoscale spatiotemporal variability of North American monsoon rainfall over complex terrain. J. Clim. 20 (9), 1751–1773.

Getis, A., Ord, J.K., 1992. The analysis of spatial association by use of distance statistics. Geogr. Anal. 24 (3), 189–206.

Haashemi, S., Weng, Q., Darvishi, A., Alavipanah, S., 2016. Seasonal variations ofthe surface urban heat island in a semi-arid city. Remote Sens. 8 (4), 1–17.

Hafner, J., Kidder, S.Q., 1999. Urban heat island modeling in conjunction with satellite-derived surface/soil parameters. J. Appl. Meteorol. 38 (4), 448–465.

Harlan, S.L., Chowell, G., Yang, S., Petitti, D.B., Morales Butler, E.J., Ruddell, B.L., Ruddell, D.M., 2014. Heat-related deaths in hot cities: estimates of human tolerance to high temperature thresholds. Int. J. Environ. Res. Public Health 11 (3), 3304–3326.

Hernández, G., Velásquez, S., 2014. Vivienda y calidad de vida. Medición del hábitat social en el México Occidental. Rev. Bitácora Urbano Territorial 24 (1), 1–36.
Hu, K., Yang, X., Zhong, J., Fei, F., Qi, J., 2017. Spatially explicit mapping of heat health risk utilizing environmental and socioeconomic data. Environ. Sci. Technol. 51 (3), 1498–1507.
Instituto Municipal de Planeación (IMPLAN), 2014. Programa de Desarrollo Urbano del Centro de Población de Hermosillo. Hermosillo. pp. 286 Available online: http://www.implanhermosillo.gob.mx/wp-content/uploads/2017/08/PDUCPH-2014.pdf (accessed on March 8, 2019).
Instituto Nacional de Estadística Geografía e Informática (INEGI), 2010. XII Censo Nacional de Población y Vivienda. Instituto Nacional de Estadística, Geografía e Informática. Available online, Aguascalientes. https://www.inegi.org.mx/programas/ccpv/2010/ (accessed on March 8, 2019).
Instituto Nacional de Estadística Geografía e Informática (INEGI), 2015. Principales resultados de la Encuesta Intercensal 2015 : Sonora. Instituto Nacional de Estadística y Geografía, México.
Irons, J.R., Dwyer, J.L., Barsi, J.A., 2012. The next Landsat satellite: the Landsat data continuity mission. Remote Sens. Environ. 122, 11–21.
Isobe, A., Uchida, K., Tokai, T., Iwasaki, S., 2015. East Asian seas: a hot spot of pelagic microplastics. Mar. Pollut. Bull. 101, 618–623.
Jacobs, J.M., Mohanty, B.P., Hsu, E.C., Miller, D., 2004. Field scale variability, time stability and similarity of soil moisture. Remote Sens. Environ. 92 (4), 436–446.
Jenerette, G.D., Harlan, S.L., Stefanov, W.L., Martin, C.A., 2011. Ecosystemservices and urban heat riskscape moderation: water, green spaces, and social inequality in Phoenix, USA. Ecol. Appl. 21 (7), 2637–2651.
Jenerette, G.D., Harlan, S.L., Buyantuev, A., Stefanov, W.L., Declet-Barreto, J., Ruddell, B.L., Myint, S.W., Kaplan, S., Li, X., 2016. Micro-scale urban surface temperatures are related to land-cover features and residential heat related health impacts in Phoenix, AZ USA. Landsc. Ecol. 31 (4), 745–760.
Kroeger, T., McDonald, R.I., Boucher, T., Zhang, P., Wang, L., 2018. Where the people are: current trends and future potential targeted investments in urban trees for PM 10 and temperature mitigation in 27 US Cities. Landsc. Urban Plan. 177, 227–240.
Lazzarini, M., Molini, A., Marpu, P.R., Ouarda, T.B., Ghedira, H., 2015. Urban climate modifications in hot desert cities: the role of land cover, local climate, and seasonality. Geophys. Res. Lett. 42 (22), 9980–9989.
Li, W., Cao, Q., Lang, K., Wu, J., 2017. Linking potential heat source and sink to urban heat island: heterogeneous effects of landscape pattern on land surface temperature. Sci. Total Environ. 586, 457–465.
Li, H., Zhou, Y., Li, X., Meng, L., Wang, X., Wu, S., Sodoudi, S., 2018. A new method to quantify surface urban heat island intensity. Sci. Total Environ. 624, 262–272.
Liu, L., Zhang, Y., 2011. Urban heat island analysis using the Landsat TM data and ASTER data: A case study in Hong Kong. Remote Sens. 3 (7), 1535–1552.
Lo, C.P., Quattrochi, D.A., Luvall, J.C., 1997. Application of high-resolution thermal infrared remote sensing and GIS to assess the urban heat island effect. Int. J. Remote Sens. 18 (2), 287–304.
Loughnan, M., Nicholls, N., Tapper, N.J., 2012. Mapping heat health risks in urban areas. Int. J. Popul. Res. 2012, 1–12.
Martínez-Austria, P., Bandala, E., 2017. Temperature and heat-related mortality trends in the Sonoran and Mojave Desert Region. Atmosphere 8 (3), 53–65.
Mathew, A., Khandelwal, S., Kaul, N., 2016. Spatial and temporal variations of urban heat island effect and the effect of percentage impervious surface area and elevation on land surface temperature: study of Chandigarh city, India. Sustain. Cities Soc. 26, 264–277.
Mathew, A., Khandelwal, S., Kaul, N., 2017. Investigating spatial and seasonal variations of urban heat island effect over Jaipur city and its relationship with vegetation, urbanization and elevation parameters. Sustain. Cities Soc. 35, 157–177.
Myint, S.W., Zheng, B., Talen, E., Fan, C., Kaplan, S., Middel, A., Smith, M., Huang, H., Brazel, A., 2015. Does the spatial arrangement of urban landscape matter? Examples of urban warming and cooling in Phoenix and Las Vegas. Ecosyst. Health Sustain. 1 (4), 1–15.
Navarro-Estupiñan, J., Robles-Morua, A., Vivoni, E.R., Zepeda, J., Montoya, J., Verduzco, V.V., 2018. Observed trends and future projections of extreme heat events in Sonora, Mexico. Int. J. Climatol. 38 (14), 5158–5181.
Ord, J., Getis, A., 1995. Local spatial autocorrelation statistics: distributional issues. Geogr. Anal. 27 (4), 286–306.
Peeters, A., Zude, M., Käthner, J., Ünlü, M., Kanber, R., Hetzroni, A., Gebbers, R., Ben-Gal, A., 2015. Getis–Ord's hot- and cold-spot statistics as a basis for multivariate spatial clustering of orchard tree data. Comput. Electron. Agric. 111, 140–150.
Peng, J., Jia, J., Liu, Y., Li, H., Wu, J., 2018. Seasonal contrast of the dominant factors for spatial distribution of land surface temperature in urban areas. Remote Sens. Environ. 215, 255–267.
Ranagalage, M., Estoque, R., Murayama, Y., 2017. An urban heat island study of the Colombo Metropolitan Area, Sri Lanka, based on Landsat Data (1997–2017). Int. J. Geo-Inf. 6, 189–205.
Reid, C.E., O'Neill, M.S., Gronlund, C.J., Brines, S.J., Brown, D.G., Diez-Roux, A.V., Schwartz, J., 2009. Mapping community determinants of heat vulnerability. Environ. Health Perspect. 117 (11), 1730–1736.
Smith, E.R., Tran, L.T., O'Neill, R., Locantore, N., 2003. *Regional Vulnerability* Assessment for the Mid-Atlantic Region: Evaluation of Integration Methods *and Assessment Results*. US Environmental Protection Agency, Washington DC, pp. 1–83 EPA/600/R-03/082 (NTIS PB2004-104952).
Song, J., Wang, Z.H., Myint, S.W., Wang, C., 2017. The hysteresis effect on surface-air temperature relationship and its implications to urban planning: An examination in Phoenix, Arizona, USA. Landsc. Urban Plan. 167, 198–211.
Steeneveld, G.J., Koopmans, S., Heusinkveld, B.G., Van Hove, L.W.A., Holtslag, A.A.M., 2011. Quantifying urban heat island effects and human comfort for citiesof variable size and urban morphology in the Netherlands. J. Geophys. Res. 116 (D20), 1–14.
Tang, Q., Vivoni, E.R., Munoz-Arriola, F., Lettenmaier, D.P., 2012. Predictability of evapotranspiration patterns using remotely-sensed vegetation dynamics during the North American monsoon. J. Hydrometeorol. 13, 103–121.
Tang, J., Di, L., Xiao, J., Lu, D., Zhou, Y., 2017. Impacts of land use and socio-economic patterns. Int. J. Remote Sens. 38 (11), 3445–3465.
Templeton, N.P., Vivoni, E.R., Wang, Z., Schreiner-McGraw, A.P., 2018. Quantifying water and energy fluxes over different urban land covers in Phoenix, Arizona. J. Geophys. Res.-Atmos. 123 (4), 2111–2128.
USGS, December 2014. LANDSAT Surface Reflectance-Derived Spectral Indices (accessed on March 8, 2019). Available online: https://landsat.usgs.gov/sites/default/files/documents/si_product_guide.pdf.
Vachaud, G., Passerat de Silans, A., Balabanis, P., Vauclin, M., 1985. Temporal stability of spatially measured soil water probability density function1. Soil Sci. Soc. Am. J. 49 (4), 822–828.
Vivoni, E.R., Gebremichael, M., Watts, C.J., Bindlish, R., Jackson, T.J., 2008. Comparison of ground-based and remotely-sensed surface soil moisture estimates over complex terrain during SMEX04. Remote Sens. Environ. 112 (2), 314–325.
Wang, C., Myint, S., Wang, Z., Song, J., 2016. Spatio-temporal modeling of the urban heat island in the Phoenix metropolitan area: land use change implications. Remote Sens. 8 (3), 185–201.
Weng, Q., Lu, D., Schubring, J., 2004. Estimation of land surface temperature–vegetation abundance relationship for urban heat island studies. Remote Sens. Environ. 89 (4), 467–483.
World Health Organization, 2010. Urban Planning, Environment and Health: From Evidence to Policy Action, Meeting Report. World Health Organization, Copenhagen, Denmark, Copenhagen, pp. 1–119.
Xiang, T.T., Vivoni, E.R., Gochis, D.J., 2014. Seasonal evolution of ecohydrological controls on land surface temperature over complex terrain. Water Resour. Res. 50 (5), 3852–3874.
Xiang, T.T., Vivoni, E.R., Gochis, D., Mascaro, G., 2017. On the diurnal cycle of surface energy fluxes in the North American monsoon region using the WRF-Hydro modeling system. J. Geophys. Res. 122 (17), 9024–9049.
Yang, C., He, X., Yan, F., Yu, L., Bu, K., Yang, J., Chang, L., Zhang, S., 2017. Mapping the influence of land use/land cover changes on the urban heat island effect—a case study of Changchun, China. Sustainability 9 (2), 1–17.
Zanter, K. (2016). Landsat 8 data users handbook. Landsat Science Official Website. Available online: https://landsat. usgs. gov/landsat-8-l8-data-users-handbook (accessed on March 1, 2019).